Stiffness Tuning with Bias Magnetic Fields in Ferromagnetic Shape Memory Ni–Mn–Ga

NEELESH N. SARAWATE AND MARCELO J. DAPINO*

Department of Mechanical Engineering, The Ohio State University, E340, Scott Laboratory
201 West 19th Avenue, Columbus, OH 43210, USA

ABSTRACT: This article presents the dynamic characterization of mechanical stiffness changes under varied bias magnetic fields in single-crystal ferromagnetic shape memory Ni–Mn–Ga. The material is first converted to a single variant through the application and subsequent removal of a bias magnetic field. Mechanical base excitation is then used to measure the acceleration transmissibility across the sample, from where the resonance frequency is directly identified. The tests are repeated for various longitudinal and transverse bias magnetic fields ranging from 0 to 575 kA/m. A SDOF model for the Ni–Mn–Ga sample is used to calculate the mechanical stiffness and damping from the transmissibility measurements. An abrupt resonance frequency increase of 21% and a stiffness increase of 51% are obtained with increasing longitudinal fields. A gradual resonance frequency change of −35% and a stiffness change of −61% are obtained with increasing transverse fields. A constitutive model is implemented which describes the dependence of material stiffness on transverse bias magnetic fields. The damping exhibited by the system is low in all cases (≈ 0.03). The measured dynamic behaviors make Ni–Mn–Ga well suited for vibration absorbers with electrically tunable stiffness.

Key Words: ferromagnetic shape memory, Ni–Mn–Ga, stiffness tuning, dynamic characterization, vibration control.

INTRODUCTION

FERROMAGNETIC shape memory alloys (FSMAs) in the Ni–Mn–Ga system generate magnetic field induced strain of 6%, which is about 100 times greater than the strain generated by magnetostrictive and piezo-electric materials. Due to the magnetic field activation, FSMAs exhibit faster response than thermally activated shape memory alloys, at comparable strain magnitudes. The combination of large strain and broad frequency bandwidth makes FSMAs attractive for actuation applications (Kiang and Tong, 2005; Soderberg et al., 2005). The high saturation field ($\sim$400 kA/m) and low blocking stress ($<$3 MPa) of single-crystal Ni-Mn-Ga limits its useful actuation range, although recent studies have shown promising new FSMAs with higher blocking force (Karaca et al., 2006).

FSMA applications other than actuation have received limited attention. Studies have shown the viability of Ni–Mn–Ga in sensing and energy harvesting applications (Suorsa et al., 2004; Karaman et al., 2007; Sarawate and Dapino, 2007a). As a sensor material,

Ni–Mn–Ga has been shown to exhibit a reversible magnetization change of 0.15 T when compressed by 5.8% strain at a bias field of 368 kA/m (Sarawate and Dapino, 2007a). In addition, the stiffness of Ni–Mn–Ga varies with externally applied fields and stresses. In the low temperature martensitic phase, application of a sufficiently large transverse magnetic field ($>$700 kA/m) produces a Ni–Mn–Ga microstructure with a single 'field preferred' variant configuration (Figure 1(b)); application of a sufficiently large longitudinal field ($>$350 kA/m) or sufficiently large compressive stress ($>$3 MPa) creates a single 'stress preferred' variant configuration (Figure 1(c)). The quasistatic stress–strain curve for Ni–Mn–Ga (Sarawate and Dapino, 2007a) shows that the two configurations have significantly different stiffness. At intermediate fields and stresses, both variants coexist and the material exhibits a bulk stiffness between the two extreme values (Figure 1(a)). This microstructure offers the opportunity to control the bulk material stiffness through the vary of variant volume fractions with magnetic fields or stresses. Magnetic fields are the preferred method for stiffness control as they can be applied remotely and can be adjusted precisely. Faidley et al. (2006) investigated stiffness changes in research grade, single crystal Ni–Mn–Ga driven with magnetic fields applied along

---
*Author to whom correspondence should be addressed.
E-mail: dapino.1@osu.edu
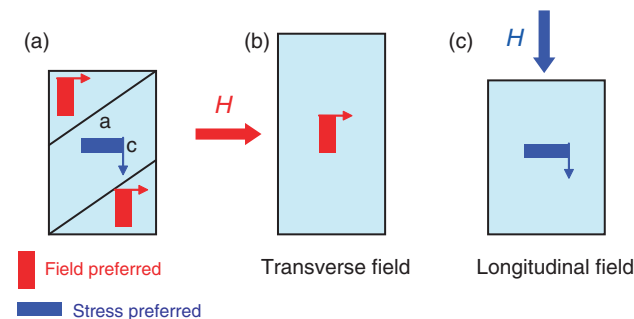Figures 1–3, 5–9, 14 and 15 appear in color online: http://jim.sagepub.com

Figure 1. *(a) simplified 2D twin variant microstructure of Ni-Mn-Ga. (b) microstructure after application of a sufficiently high transverse magnetic field. (c) after application of a sufficiently high longitudinal field.*

Figure 2. *Schematic of the longitudinal field test setup.*

Figure 3. *Schematic of the transverse field test setup.*

the [001] (longitudinal) direction. The material used in that study exhibits reversible field induced strain when the longitudinal field is removed, which is attributed to internal bias stresses associated with pinning sites. The fields were applied with permanent magnets bonded onto the material, which makes it difficult to separate resonance frequency changes due to magnetic fields or mass increase. Analytical models were developed to address this limitation.

In this study we isolate the effect of magnetic field on the stiffness of Ni–Mn–Ga by applying the magnetic fields in a non-contact manner, and investigate the stiffness characteristics under both longitudinal and transverse magnetic fields. Base excitation is used to measure the acceleration transmissibility across a prismatic Ni–Mn–Ga sample, from where its resonance frequency is directly identified. Prior to the transmissibility measurements, a stress-preferred or field-preferred variant configuration is established through the application and subsequent removal of a bias field using a solenoid coil or an electromagnet, respectively. We show that longitudinal and transverse bias magnetic fields have drastically different effects on the stiffness of Ni–Mn–Ga: varying the former produces two distinct stiffness states whereas varying the latter produces a continuous range of stiffnesses. We present a constitutive model that describes the continuous stiffness variation.

EXPERIMENTAL SETUP AND PROCEDURE

The measurements are conducted on commercial single crystal Ni–Mn–Ga manufactured by Adaptamat, Inc. A sample with dimensions 6 mm × 6 mm × 10 mm is tested in its low-temperature martensite phase. The sample exhibits 5.8% free strain when exposed to transverse fields of ~400 kA/m. The broadband mechanical excitation is provided by a Labworks ET126-B shaker table which has a frequency range of 0 to 8500 Hz and a 25 lb peak sine force capability. The shaker is driven by an MB Dynamics SL500VCF power amplifier which has a power rating of 1000 VA and maximum voltage gain of
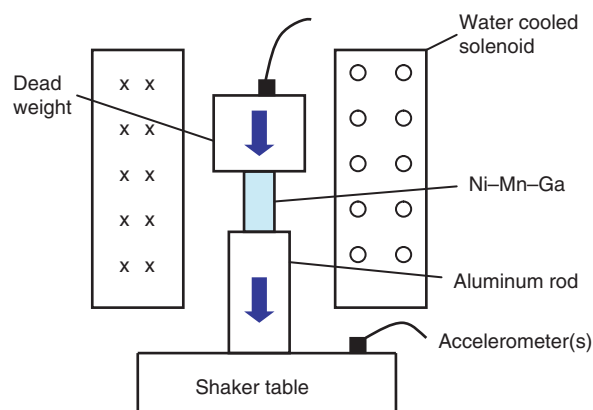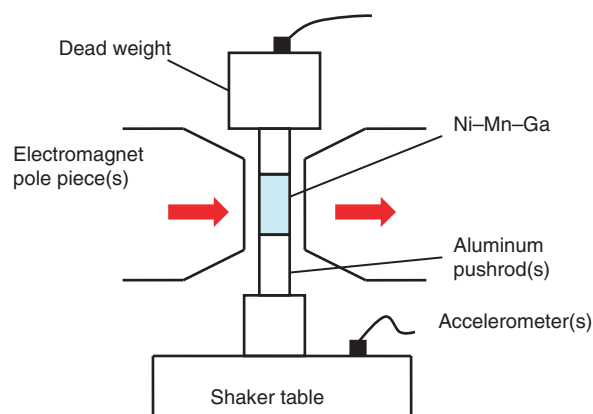
48 with 40 V peak and 16 A rms. The shaker is controlled by a Data Physics SignalCalc 550 vibration controller.

A schematic of the test setup for longitudinal field measurements is shown in Figure 2. The sample is mounted on an aluminum pushrod fixed on the shaker table; a dead weight is mounted on top of the sample. Two PCB accelerometers measure the base and top accelerations. The longitudinal field is applied by a custom-made water cooled solenoid transducer which is made from AWG 15 insulated copper wire with 28 layers and 48 turns per layer (Malla et al., 2006). The solenoid is driven by two Techron 7790 amplifiers connected in series which produce an overall voltage gain of 60 and a maximum output current of 56 A into the 3.7 Ω coil. The solenoid has a magnetic field rating of 11.26 (kA/m)/A.

The transverse field experiment is illustrated in Figure 3. The magnetic fields are applied by a custom-made electromagnet made from laminated E-cores with 2 coils of about 550 turns each made from AWG 16 magnet wire. The coils are connected in parallel. The electromagnet, which has a magnetic field rating of 63.21 (kA/m)/A, can produce fields of up to 750 kA/m.

For the longitudinal field tests, the sample is initially configured as a single field-preferred variant.

The sample microstructure can be changed with increasing longitudinal fields by favoring the growth of stress-preferred variants, which results in stiffening with increasing magnetic field. The sample in zero-field condition is first subjected to band-limited white noise base excitation with a frequency range from 0 to 4000 Hz and reference RMS acceleration of 0.2 g. After completion of the zero-field test, a DC voltage is applied across the solenoid to produce a DC longitudinal magnetic field on the sample. Due to the fast response of Ni–Mn–Ga (Marioni et al., 2003), application of the field for a small time period is enough to change the variant configuration. In this study we apply the fields for ∼1–2 s. If the field is strong enough to initiate twin boundary motion, stress-preferred variants are generated from the original field-preferred variants. The sample is again subjected to band-limited white noise base excitation from which the transfer function between the top and base acceleration is obtained. This process is continued until the sample reaches a complete stress-preferred variant state.

For the transverse field tests, the sample is initially configured as a single stress-preferred variant. This configuration is obtained by applying a high longitudinal field in excess of 400 kA/m. The sample is mounted on the shaker table between the pole faces of the electromagnet using aluminum pushrods, and a dead weight is mounted on the top of the sample. The test procedure is the same as in the longitudinal field test: the transverse bias field is incremented by a small amount and subsequently removed before each run. When the field is sufficiently high, field-preferred variants are generated at the expense of stress-preferred variants, resulting in a change in stiffness and resonance frequency.

THEORY

The system is represented by the single degree of freedom (SDOF) spring-mass-damper model shown in Figure 4, where K_s represents the stiffness of the Ni–Mn–Ga sample, K_r is the total stiffness of the aluminum pushrods, M is the dead weight on the sample, and C is the overall damping present in the system. The base motion is represented by x, and the top motion is represented by y.

The system is subjected to band-limited white noise base excitation with reference acceleration to the shaker controller having an RMS value of 0.2 g. The reference acceleration has uniform autospectral density (PSD) over the range from 0 to 4000 Hz:

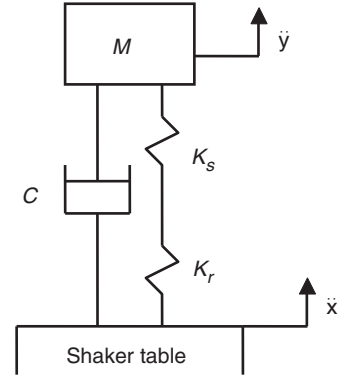$$G_{rr}(f) = G \quad 0 \leq f \leq 4000$$
$$= 0 \quad f > 4000, \tag{1}$$

Figure 4. *SDOF spring-mass-damper model used for characterization of the Ni–Mn–Ga material.*
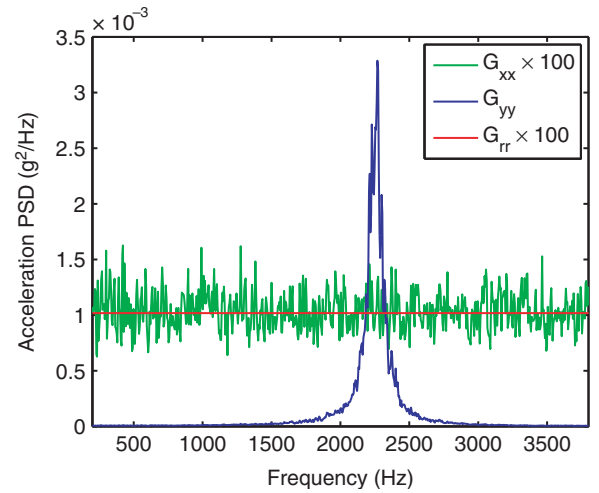

Figure 5. *Experimentally obtained acceleration PSDs.*

with f the frequency (Hz), G_{rr} the reference acceleration PSD (g²/Hz), and G the constant value of reference acceleration PSD (g²/Hz) over the given frequency band. The measured base acceleration PSD, or actual input acceleration PSD, differs from the reference PSD and is denoted by G_{xx} (g²/Hz). The top acceleration PSD is denoted by G_{yy} (g²/Hz). The RMS acceleration values are related to the corresponding acceleration PSDs by

$$\psi_r^2 = \int_{f_{min}}^{f_{max}} G_{rr}(f) df,$$
$$\psi_x^2 = \int_{f_{min}}^{f_{max}} G_{xx}(f) df, \tag{2}$$
$$\psi_y^2 = \int_{f_{min}}^{f_{max}} G_{yy}(f) df,$$

where ψ_r, ψ_x, ψ_y represent the reference, input, and output RMS acceleration (m/s²) values, respectively. Frequencies f_{min} and f_{max}, represent the lower and upper limits of the band limited signal, respectively. Figure 5 shows the experimentally obtained PSDs for

input, output, and reference acceleration signals in one of the test runs. In this case, the RMS acceleration values obtained from (2) are $\psi_r = 0.2\,\text{g}^2/\text{Hz}$, $\psi_x = 0.2036\,\text{g}^2/\text{Hz}$, and $\psi_y = 0.7048\,\text{g}^2/\text{Hz}$. It is noted that the measured input PSD does not have an exactly uniform profile as the reference PSD does. However, the RMS values for the input and reference PSDs differ by <2%.

Since the cross-PSD between the input and output signals (G_{xy}) cannot be measured by the shaker controller, only the magnitude (and not the phase) of the transfer function between the top and base acceleration signals are obtained experimentally. The transfer function magnitude calculated from the experimental data is given as

$$|H_{xy}(f)|^2 = \frac{G_{yy}}{G_{xx}}, \qquad (3)$$

where $H_{xy}(f)$ represents the experimentally obtained transfer function between the top and base accelerations. For the SDOF system shown in Figure 4, the transfer function between the top and base acceleration is given as

$$H(f) = \frac{1 + j(2\zeta f/f_n)}{1 - (f/f_n)^2 + j(2\zeta f/f_n)}, \qquad (4)$$

where ζ is the overall damping ratio of the system and f_n is the natural frequency of the system (Hz). The natural frequency is experimentally obtained as the frequency at which the output PSD is maximum,

$$f_n = \arg\max_f [G_{yy}(f)]. \qquad (5)$$

If the system in Figure 4 is subjected to band-limited input acceleration of uniform PSD G, the RMS value of output acceleration is given as (Bendat and Piersol, 2000),

$$\psi_y^2 = \frac{G\pi f_n(1 + 4\zeta^2)}{4\zeta}. \qquad (6)$$

Although the measured input acceleration PSD is not uniform, it can be assumed to be uniform with sufficient accuracy for calculation of the damping ratio. An expression for the damping ratio is given as

$$\zeta = \frac{\psi_y^2 - \sqrt{(\psi_y^2)^2 - (G\pi f_n)^2}}{2\,G\pi f_n}, \qquad (7)$$

where the RMS value of output acceleration (ψ_y) is obtained from the measured output PSD (G_{yy})

from (2), f_n is obtained from (5), and G is the uniform reference PSD. The experimental and calculated transfer function for the case under consideration are shown in Figure 6. It is noted that the assumption of a linear, SDOF spring-mass-damper system, and the approximation of using the reference acceleration PSD to calculate the effective damping ratio work well for describing the experimentally obtained transfer function. Further, the analytical expression for the natural frequency of the system is given as,

$$f_n = \frac{1}{2\pi}\sqrt{\frac{K_s K_r}{(K_s + K_r)M}}, \qquad (8)$$

from where the mechanical stiffness of the Ni–Mn–Ga sample is obtained as,

$$K_s = \frac{M(2\pi f_n)^2 K_r}{K_r - M(2\pi f_n)^2}. \qquad (9)$$

Further, the viscous damping coefficient has the form

$$C = 2\zeta\sqrt{KM}. \qquad (10)$$

The stiffness change and resonance frequency change are calculated with respect to the initial material stiffness, which depends on whether the test involves longitudinal or transverse fields. The stiffness change is given by

$$\Delta K_s = \frac{K_s - K_{s0}}{K_{s0}} \times 100, \qquad (11)$$

where ΔK_s is the overall stiffness change (%), and K_{s0} is the initial, zero-field stiffness.
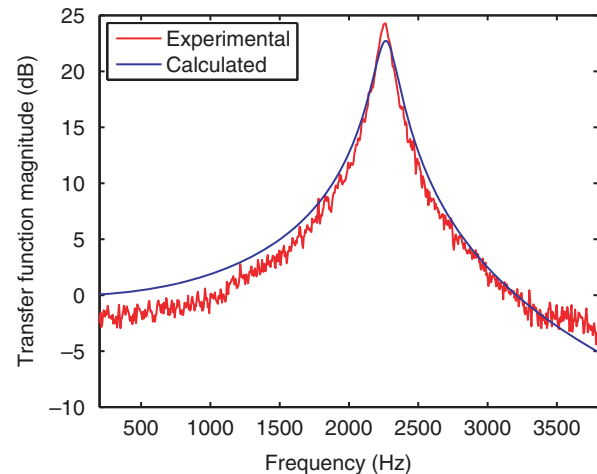

Figure 6. *Transfer function between top and base accelerations.*

RESULTS AND DISCUSSION

Longitudinal Field Tests

The transmissibility ratio transfer function relating the acceleration of the top to the acceleration of the base provides information on the resonance frequency and damping present in the system. The measurements obtained in the longitudinal field configuration are shown in Figure 7 for one of the test runs. The sample exhibits only two distinct resonances after subjecting it to several fields ranging from 0 to 462 kA/m. At fields below 330 kA/m, the sample exhibits a resonance frequency of approximately 1913 Hz; at fields of more than 330 kA/m, the resonance is observed at 2299 Hz. These results point to an ON/OFF effect with a threshold field of 330 kA/m. This result was validated through repeated runs under the same conditions, as shown in Figure 8, which shows the two distinct resonances for three different tests as well as calculations.

The stiffness of the aluminum pushrod used in these tests is 1.36e8 N/m, and the mass of the dead weight is 60.97 g. The two average stiffnesses calculated with expression (9) are $K_{s1} = 9.33e6$ N/m and $K_{s2} = 1.41e7$ N/m. The average damping ratios calculated with expression (7) are $\zeta_1 = 0.0334$ and $\zeta_2 = 0.0422$. The average field at which the resonance shift takes place is 285 kA/m. The variation in the field at which the threshold occurs may be due to small variations in the position of the sample with respect to the solenoid. If the sample is not exactly aligned along the length of the solenoid, the effective field in the sample might change. This can give rise to varied magnitudes of field even when the current in the solenoid is the same.

A field of 330 kA/m can be considered optimum for achieving the second resonance frequency as compared to the resonance at lower fields. The results of the longitudinal tests are summarized in Table 1. It is seen that there is an average resonance shift of 20.9% and an average stiffness shift of 51.0%, both relative to the zero-field value. The stiffness increases with increasing field since the sample is initially in its field-preferred, mechanically softest state. Although the damping ratios also show a large average shift of 26.7%, the damping values are small at all magnetic fields. This is beneficial for the implementation of Ni–Mn–Ga in tunable vibration absorbers with a targeted absorption frequency.

Transverse Field Tests

The measurements conducted in the transverse field case are shown in Figure 9 for one of the test runs. Two differences with respect to the longitudinal tests are observed. First, since the sample is initially configured in its stiffest state as a single stress-preferred variant, an increase in transverse magnetic field produces a decrease in the mechanical stiffness and associated resonance frequency. Secondly, the material exhibits a gradual change in resonance frequency with changing field, in this case from values of ~2300 Hz for zero applied field to ~1430 Hz for a DC magnetic field of 439 kA/m. Further, the effective resonance frequency change from 2300 to 1430 Hz occurs for a relatively narrow field range from 245 kA/m to 439 kA/m. Similar behavior was identified after conducting several test runs, three of which are considered here for estimating the relevant model parameters. The frequency shifts for the three cases are −36.4, −33.0, and −35.9%, giving an average shift of −35.1% between the extreme values (see Table 2).

The overall resonance frequency shift and sample stiffness shift in the transverse field tests are higher than in the longitudinal field test. For the longitudinal measurements, the average sample stiffness in the
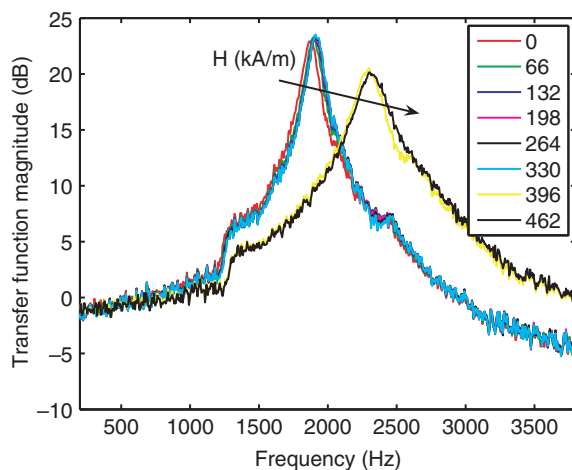

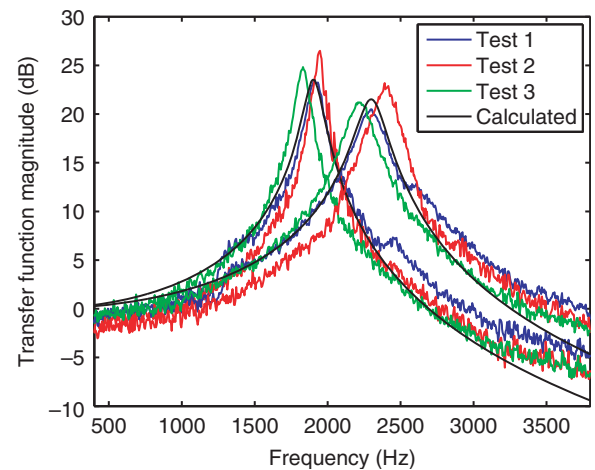**Figure 7.** *Acceleration transmissibility with longitudinal field.*

Figure 8. *Longitudinal field test model results and repeated measurements under the same field inputs.*

Table 1. Summary of longitudinal field test results.

Run#	f_{n1} (Hz)	f_{n2} (Hz)	Δf_n (%)	K_{s1} (N/m)	K_{s2} (N/m)	ΔK_s (%)	ζ_1	ζ_2	$\Delta \zeta$ (%)
1	1902	2299	**20.9**	9.31e6	1.40e7	**50.8**	0.035	0.046	**32.0**
2	1963	2401	**22.3**	9.96e6	1.54e7	**55.1**	0.030	0.038	**28.1**
3	1846	2207	**19.6**	8.73e6	1.28e7	**51.0**	0.036	0.043	**20.0**
Avg.			**20.9**			**51.0**			**26.7**
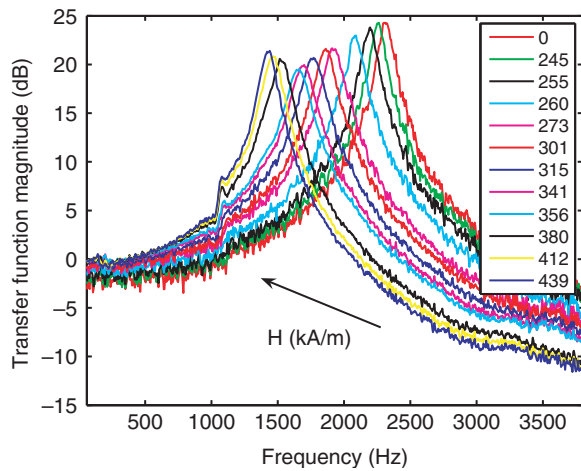
Figure 9. *Transmissibility ratio measurements with transverse field configuration.*

stress-preferred configuration is 1.38e7 N/m, whereas for the transverse tests is 1.34e7 N/m. However, the average stiffness when the sample is supposed to be in the completely field-preferred state is 9.1e6 N/m in the case of longitudinal field tests and 5.27e6 N/m in the case of transverse field tests. This state occurs at the start for the longitudinal field test and at the end in the transverse field test. The possible reason behind this difference is that the manual pressure applied while mounting the sample for longitudinal field tests results in initiation of twin boundary motion and a certain fraction of the sample is transformed into the stress-preferred variant. This results in an increased stiffness as compared to a completely field-preferred configuration. However, this behavior is consistent in the three runs indicating that the structure assumed by the sample had been nearly the same during the tests. The sample stiffness and the overall system damping ratio are calculated as detailed in the previous section 6. The aluminum pushrods used in these tests have different dimensions than those used in the longitudinal measurements, and hence the stiffness has a different value of 1.068e7 N/m. The dead weight has the same mass of 60.87 g. Table 2 shows the resonance frequency, stiffness, and damping ratio variation in extreme values for the transverse field tests.

The damping ratio, viscous damping coefficient and resonance frequency variations with initial bias field for the test run in Figure 9 are shown in Figures 10–12, respectively. The damping ratios are small, hence the

material is suitable for tunable vibration absorption applications. It is also noted that the damping ratio values are relatively flat over the bias fields. The slight rise and drop in the damping can be attributed to the presence of twin boundaries (Gans and Carman, 2004). With increasing bias field, twin boundaries are created which leads to increased damping. At high bias fields, the sample is converted to a complete field-preferred state. In this condition, the number of twin boundaries decreases again, resulting in relatively lower damping. Figure 10 shows this trend: the damping coefficient is maximum at intermediate fields, and attains relatively lower values at the lowest and highest fields.

The variation of stiffness with changing bias field is modeled with an existing continuum thermodynamics model developed by Sarawate et al. (Sarawate and Dapino, 2007a, 2007b). This model was developed to describe the sensing behavior of Ni–Mn–Ga, hence emphasis was placed on accurately describing the effect of stress on magnetization. Prior thermodynamic models on Ni–Mn–Ga (Hirsinger and Lexcellent, 2003; Kiefer and Lagoudas, 2005; Faidley et al., 2008) were primarily developed for describing the actuation behavior and thus did not quantify the magnetization response.

The net compliance of the Ni–Mn–Ga sample is given by a linear combination of the field-preferred and stress-preferred volume fractions, see Figure 13(b). Thus, the net material modulus is,

$$E(\xi) = \frac{1}{S(\xi)} = \frac{1}{S_0 + (1 - \xi)(S_1 - S_0)}, \qquad (12)$$

where S is the net compliance, S_0 is the compliance of the material in complete field-preferred state, and S_1 is the compliance of the material in complete stress-preferred state. The twin variants are separated by a twin boundary, and each side of the twin boundary contains a specific variant. If the bulk material is subjected to a force, the stiffnesses associated with the stress-preferred and field-preferred variants will be under equal forces, i.e., the two stiffnesses will be in series. Therefore, the net compliance of the system is assumed to be a linear combination of the compliances of the field-preferred and stress-preferred variants.

With increasing transverse field, the Ni–Mn–Ga sample starts deforming because its twin variant

Table 2. Summary of transverse field test results.

Run#	f_{n1} (Hz)	f_{n2} (Hz)	Δf_n (%)	K_{s1} (N/m)	K_{s2} (N/m)	ΔK_s (%)	ζ_1	ζ_2	$\Delta\zeta$ (%)
1	2294	1460	**−36.4**	1.41e7	0.53e7	**−62.5**	0.030	0.037	**24.5**
2	2147	1439	**−33.0**	1.21e7	0.51e7	**−57.7**	0.032	0.037	**15.5**
3	2294	1470	**−35.9**	1.41e7	0.54e7	**−61.9**	0.030	0.046	**55.6**
Avg.			**−35.1**			**−60.7**			**31.8**
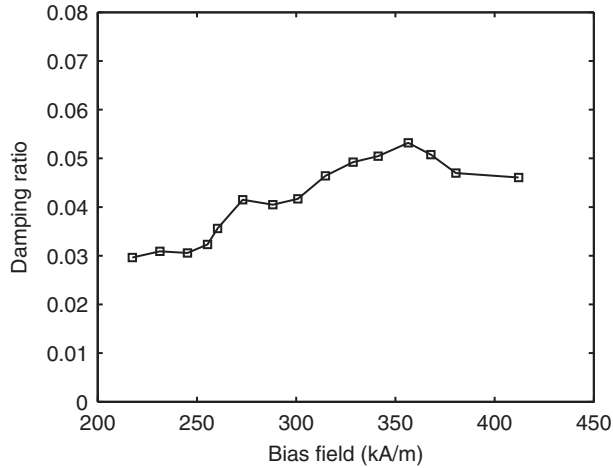
Figure 10. Variation of damping ratio with initial transverse bias field.
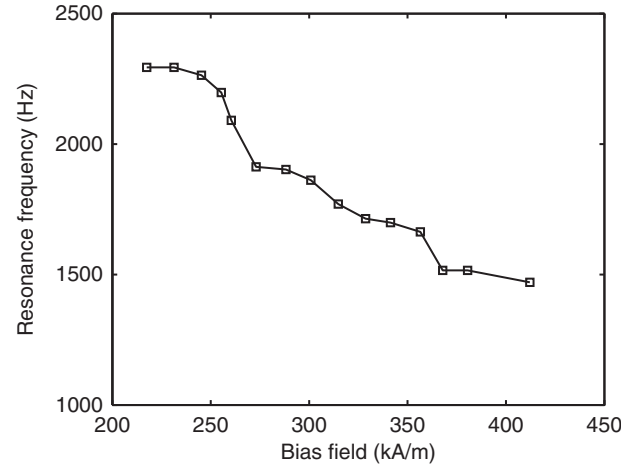
Figure 12. Variation of resonance frequency with initial transverse bias field.
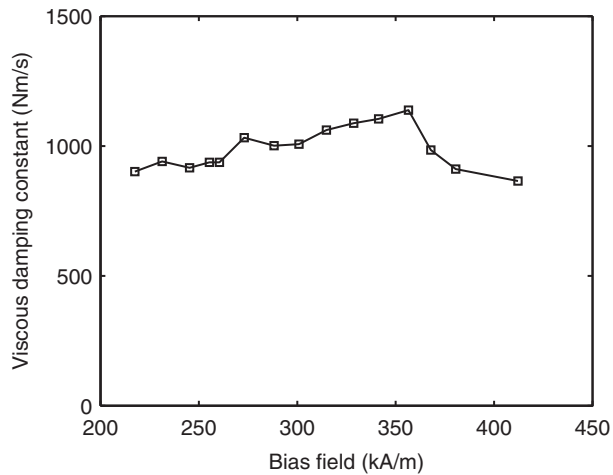
Figure 11. Variation of viscous damping coefficient with initial transverse bias field.

configuration changes. The variation of the field-preferred (ξ) and stress-preferred ($1-\xi$) martensite volume fractions with field is described by the magnetomechanical constitutive model. The model is formulated by writing a thermodynamic Gibbs energy potential consisting of magnetic and mechanical components. The magnetic energy has Zeeman, anisotropy, and magnetostatic contributions; the mechanical energy has elastic and twinning energy contributions. Mechanical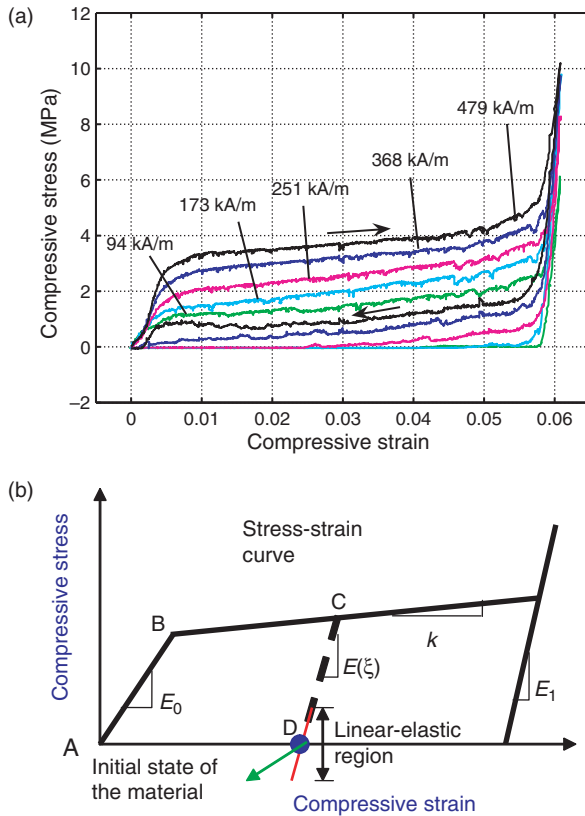 dissipation and the microstructure of Ni–Mn–Ga are incorporated in the continuum thermodynamics framework by considering the internal state variables volume fraction, domain fraction, and magnetization rotation angle. The constitutive strain response of the material is obtained by restricting the process through the second law of thermodynamics, as detailed in (Sarawate and Dapino, 2007b). The model is summarized in Table 3.

As shown in Figure 13(a), the constitutive response of Ni–Mn–Ga is nonlinear and hysteretic only when the applied field or stress is sufficient to overcome the energy associated with critical twinning stress. In this study, the material is subjected to base excitation when it consists of a given mixture of variants. This mixture is obtained by applying either transverse or collinear bias fields, although the same mixture could be obtained by compressing the material from a complete field-preferred state at zero field.

The initial state of the material is at zero stress, as represented by point D in Figure 13(b). Base excitation induces compressive and tensile stresses in the material. However, the magnitude of these stresses is very small since the applied excitation is of small magnitude. These stresses are not sufficient to overcome the energy associated with the twinning stress. Unless the stress exceeds the value at point C, the material exhibits linear-elastic behavior. Thus, we observe bulk material behavior which can be accurately predicted by a linear spring-mass model.
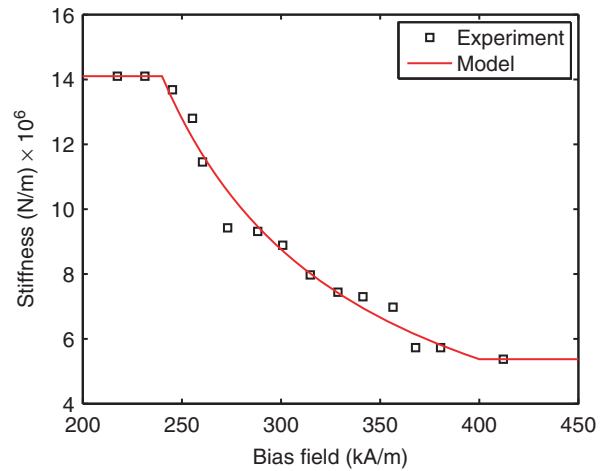
Table 3. Summary of volume fraction model (Sarawate and Dapino, 2007a, 2007b).

$$\text{Clausius-Duhem inequality: } -\rho\dot{\phi} - \dot{\sigma}\varepsilon_e - \mu_0 M\dot{H} + \sigma\dot{\varepsilon}_{tw} \geq 0 \tag{1}$$

$$\text{Gibbs energy: } \rho\varphi = \xi\left[-\mu_0 HM_s(2\alpha-1) + \frac{1}{2}\mu_0 N(M_s(2\alpha-1))^2\right]$$

$$+ (1-\xi)\left[-\mu_0 HM_s\sin\theta + \frac{1}{2}\mu_0 NM_s^2\sin^2\theta + K_u\sin^2\theta\right] \tag{2}$$

$$- \frac{1}{2}S(\xi)\sigma^2 + \frac{1}{2}a\varepsilon_0^2\xi^2$$

$$\text{Strain equation: } \varepsilon_e = -\frac{\partial(\rho\phi)}{\partial\sigma} = S(\xi)\sigma, \quad \varepsilon = \varepsilon_e + \varepsilon_0\xi \tag{3}$$

$$\text{Magnetization equation: } M = -\frac{1}{\mu_0}\frac{\partial(\rho\phi)}{\partial H} = M_s[2\xi\alpha - \xi + \sin\theta - \xi\sin\theta]$$

$$\text{Domain fraction: } \alpha = \frac{H}{2M_sN} + \frac{1}{2} \tag{4}$$

$$\text{Rotation angle: } \theta = \sin^{-1}\left(\frac{\mu_0 HM_s}{\mu_0 NM_s^2 + 2K_u}\right)$$

$$\text{Thermodynamic driving force: } \pi^{\xi^*} = -\frac{\partial(\rho\phi)}{\partial\xi} + \sigma\varepsilon_0 = \pi^\xi + \sigma\varepsilon_0 = \pi_{mag}^\xi + \pi_{mech}^\xi + \sigma\varepsilon_0 \tag{5}$$

$$\text{Solution for volume fraction: } \pi^{\xi^*} = \pi^{cr} = \sigma_{two}\varepsilon_0 \tag{6}$$

(a)

Figure 14. Variation of stiffness with initial bias field.

(b)

Figure 13. Stress–strain behavior: (a) experimental, (b) schematic at zero magnetic field.

The net stiffness is related to the modulus by

$$K_s = \frac{AE}{L}, \tag{13}$$

with A the cross-sectional area, and L the length of the Ni–Mn–Ga element. Using the constitutive model for volume fraction, and equations (12), (13), the stiffness change of the material with initial bias field can be calculated. Model calculations are shown in Figure 14 along with the experimental values. The model accurately predicts the stiffness variation with initial bias field.

Because of the relatively high demagnetization factor (0.385) in the transverse direction, it takes higher external fields to fully elongate the sample. Thus, a continuous change of resonance frequency and hence stiffness is observed with increasing bias fields. In the case of the longitudinal field tests, the demagnetization factor is 0.229. Thus, once the twin boundary motion starts, it

takes a very small range of fields to transform the sample fully into the stress-preferred state. Thus, an abrupt change in the resonance frequency and hence stiffness is seen in the longitudinal field tests. It should be noted that the figures are plotted with the applied bias field on the *x*-axis. The demagnetization factor should be considered if the relation with respect to the actual field is required.

CONCLUDING REMARKS

The single-crystal Ni–Mn–Ga sample characterized in this article exhibits varied dynamic stiffness with changing bias fields. The non-contact method of applying the magnetic fields ensures consistent testing conditions. This is an improvement over our prior work (Faidley et al., 2006), in which permanent magnets were used to apply magnetic fields along the longitudinal direction. Unlike that study, the characterization presented here was conducted on commercial Ni–Mn–Ga material, under both longitudinal and transverse drive configurations. The field is not applied throughout the duration of a given test, but only initially in order to transform the sample into a given twin variant configuration. This is an advantage of Ni–Mn–Ga over magnetostrictive materials such as Terfenol-D which require a continuous supply of magnetic field, and hence current in the electromagnetic coil, in order to maintain the required resonance frequency. A study on a 0.63-cm-diameter, 5.08-cm-long Terfenol-D rod driven within a dynamic resonator has shown that this material exhibits continuously variable resonance frequency tuning from 1375 to 2010 Hz (Flatau et al., 2000).

If a bi-directional resonance change was required, the system involving Ni–Mn–Ga would need a restoring mechanism. A magnetic field source perpendicular to the original field source could be used to maintain the advantage of low electrical energy consumption. Another option is to use a restoring spring; but the presence of the restoring spring results in reversible behavior of Ni–Mn–Ga, thus requiring a continuous source of current to maintain the field. Nevertheless, this work shows the suitability of using Ni–Mn–Ga in tunable vibration absorbers as it provides a broad resonance frequency bandwidth comparable to Terfenol-D, with the option of utilizing magnetic field pulse activation with very low-energy consumption. Twin boundary motion occurs almost instantaneously with the application of the field, and the material configuration remains unchanged unless a restoring field or stress is applied.

The overall resonance frequency and stiffness change in the transverse field tests are −35.1% and −60.7%, respectively. The equivalent values for the longitudinal field tests are 20.9 and 51.0%, respectively. The damping

values observed in the tests are small (≈ 0.03) and are conducive to the use of Ni–Mn–Ga in active vibration absorbers. An ON/OFF behavior is observed in the longitudinal field tests, whereas a continuously changing resonance frequency is observed in the transverse field tests. Thus, depending on the application and the frequency range under consideration, the sample can be operated either in transverse or longitudinal field configuration. The transverse field configuration offers more options regarding the ability to select a particular resonance frequency. The longitudinal field configuration only offers two discrete resonance frequencies, but can be implemented in a more compact manner.

The evolution of volume fraction with increasing transverse field is described by an existing continuum thermodynamics model, which is used to model the dependence of material stiffness on the initial bias field assuming a linear variation of compliance with volume fraction. The acceleration transmissibility transfer function is accurately quantified by assuming a discretized SDOF linear system. The development of a continuous dynamic model is desirable for handling different sample geometries and higher modes. Although in this study the magnetic field was switched off during the dynamic tests, development of a model with the sample immersed in an external magnetic field during testing might be useful for creating a more complete characterization of the dynamic behavior exhibited by Ni–Mn–Ga.

ACKNOWLEDGMENTS

REFERENCES

Bendat, J.S. and Piersol, A.G. 2000. "Random Data: Analysis & Measurement Procedures," John Wiley & Sons.

Faidley, L.E., Dapino, M.J., Washington, G.N. and Lograsso, T.A. 2006. "Modulus Increase with Magnetic Field in Ferromagnetic Shape Memory NiMnGa," *Journal of Intelligent Material Systems and Structures*, 17:123–131.

Faidley, L.E., Dapino, M.J. and Washington, G.N. 2008. "Homogenized Strain Model for NiMnGa Driven with Collinear Magnetic Field and Stress," *Journal of Intelligent Material Systems and Structures*, 19:681–694.

Flatau, A.B., Dapino, M.J. and Calkins, F.T. 2000. "High Bandwidth Tunability in a Smart Vibration Absorber," *Jorunal of Intelligent Material Systems and Structures*, 11:923–929.

Gans, H. and Carman, G.P. 2004. "High Energy Absorption in Bulk Ferromagnetic Shape Memory Alloys ($Ni_{50}Mn_{29}Ga_{21}$)," In: *Proceedings of SPIE: Smart Structures and Materials*, Vol. 5387, pp. 177–185, San Diego, CA.

Hirsinger, L. and Lexcellent, C. 2003. "Modelling Detwinning of Martensite Platelets under Magnetic and (or) Stress Actions on NiMnGa Alloys," *Journal of Magnetism and Magnetic Materials*, 254–255:275–277.

Karaca, H.E., Karaman, I., Basaran, B., Chumlyakov, Y.I. and Maier, H.J. 2006. "Magnetic Field and Stress Induced Martensite Reorientation in NiMnGa Ferromagnetic Shape Memory Alloy Single Crystals," *Acta Materialia*, 54:233–245.

Karaman, I., Basaran, B., Karaca, H.E., Karsilayan, A.I. and Chumlyakov, Y.I. 2007. "Energy Harvesting using Martensite Variant Reorientation Mechanism in a NiMnGa Magnetic Shape Memory Alloy," *Applied Physics Letters*, 90:172505-1–3.

Kiang, J. and Tong, L. 2005. "Modelling of Magneto-mechanical Behaviour of NiMnGa Single Crytals," *Journal of Magnetism and Magnetic Materials*, 292:394–412.

Kiefer, B. and Lagoudas, D.C. 2005. "Magnetic Field-induced Martensitic Variant Reorientation in Magnetic Shape Memory Alloys," *Philosophical Magazine*, 85(33–35):4289–4329.

Malla, A., Dapino, M.J., Lograsso, T.A. and Schlagel, D.L. 2006. "Large Magnetically Induced Strains in $Ni_{50}Mn_{28.7}Ga_{21.3}$ Driven with Collinear Field and Stress," *Journal of Applied Physics*, 99:063903-1–9.

Marioni, M.A., OHandley, R.C. and Allen, S.M. 2003. "Pulsed Magnetic Field-induced Actuation of NiMnGa Single Crystals," *Applied Physics Letters*, 83(19):3966–3968.

Sarawate, N. and Dapino, M. 2007a. "A Continuum Thermodynamics Model for the Sensing Effect in Ferromagnetic Shape Memory NiMnGa," *Journal of Applied Physics*, 101:123522.

Sarawate, N. and Dapino, M. 2007b. "Magnetomechanical Characterization and Unified Actuator/Sensor Modeling of Ferromagnetic Shape Memory Alloy Ni–Mn–Ga," *Proceedings of SPIE: Smart Structures and Materials*, Vol. 6526, p. 652629, San Diego, CA.

Soderberg, O., Ge, Y., Sozniov, A., Hannula, S. and Lindroos, V.K. 2005. "Recent Breakthrough Development of the Magnetic Shape Memory Effect in NiMnGa Alloys," *Smart Materials and Structures*, 14:S223–S235.

Suorsa, I., Tellinen, J., Pagounis, K. and Ullakko, E. 2004. "Voltage Generation Induced by Mechanical Straining in Magnetic Shape Memory Materials," *Journal of Applied Physics*, 95(12):8054–8058.